In vivo optophysiology reveals that G-protein activation triggers osmotic swelling and increased light scattering of rod photoreceptors

Pengfei Zhang[a], Robert J. Zawadzki[a,b,c], Mayank Goswami[a], Phuong T. Nguyen[d], Vladimir Yarov-Yarovoy[d], Marie E. Burns[b,c], and Edward N. Pugh Jr.[a,c,d,1]

[a]EyePod Small Animal Imaging Facility, University of California, Davis, CA 95618; [b]Department of Ophthalmology & Vision Science, University of California, Davis, CA 95618; [c]Cell Biology & Human Anatomy, University of California, Davis, CA 95618; and [d]Department of Physiology & Membrane Biology, University of California, Davis, CA 95618

Edited by David R. Williams, University of Rochester, Rochester, NY, and approved February 9, 2017 (received for review December 15, 2016)

The light responses of rod and cone photoreceptors have been studied electrophysiologically for decades, largely with ex vivo approaches that disrupt the photoreceptors' subretinal microenvironment. Here we report the use of optical coherence tomography (OCT) to measure light-driven signals of rod photoreceptors in vivo. Visible light stimulation over a 200-fold intensity range caused correlated rod outer segment (OS) elongation and increased light scattering in wild-type mice, but not in mice lacking the rod G-protein alpha subunit, transducin ($G\alpha_t$), revealing these responses to be triggered by phototransduction. For stimuli that photoactivated one rhodopsin per $G\alpha_t$ the rod OS swelling response reached a saturated elongation of 10.0 ± 2.1%, at a maximum rate of 0.11% s^{-1}. Analyzing swelling as osmotically driven water influx, we find the H_2O membrane permeability of the rod OS to be $(2.6 \pm 0.4) \times 10^{-5}$ cm·s^{-1}, comparable to that of other cells lacking aquaporin expression. Application of Van't Hoff's law reveals that complete activation of phototransduction generates a potentially harmful 20% increase in OS osmotic pressure. The increased backscattering from the base of the OS is explained by a model combining cytoplasmic swelling, translocation of dissociated G-protein subunits from the disc membranes into the cytoplasm, and a relatively higher H_2O permeability of nascent discs in the basal rod OS. Translocation of phototransduction components out of the OS may protect rods from osmotic stress, which could be especially harmful in disease conditions that affect rod OS structural integrity.

osmotic stress | phototransduction | optical coherence tomography | intrinsic optical signals | photoreceptor waveguiding

Optical coherence tomography (OCT) is a noninvasive, label-free light-scattering method with broad applicability in biomedicine (1, 2). OCT has been universally adopted in clinical ophthalmology to map human retinal layer structure (2) and is widely used for angiography of the eye (3) and heart (4, 5) and for in vivo biopsy of skin and other tissues (6, 7). Ocular OCT has also been used in vivo to measure "intrinsic optical signals" from the photoreceptor layer of the retina (8, 9), including from individual human cone photoreceptors (10–14). In no case, however, has the molecular mechanism underlying an intrinsic optical signal been unequivocally identified. The value of OCT in both clinical and basic science would clearly be enhanced were it possible to identify the molecular events underlying light-activated, photoreceptor-specific OCT signals.

The rod-dominant photoreceptor layer of the mouse retina is an ideal preparation for application of OCT to the investigation of macromolecular signaling mechanisms. Mouse rod outer segments (OS) are in effect genetically manipulable, femtoliter test tubes whose protein constituents (15, 16), as well as their biochemical reactions (17–19) and light-stimulated translocations (20–22), are well known and have been measured primarily with ex vivo methods. Advances in imaging technology have now made it possible to achieve subcellular-resolution imaging of the mouse retina in vivo (23–26). We recently developed a multimodal ocular imaging system for mice that combines confocal laser scanning ophthalmoscopy (SLO) and OCT (27) and used this system to quantify photoactivation (bleaching) of rhodopsin in vivo (28). Using nonstimulating near-infrared OCT we observed a photoreceptor layer-specific, bleaching-induced increase in light scattering. Here we show that this increased backscattering arises from rods, that it requires the rod G-protein alpha-subunit transducin ($G\alpha_t$), and that it is triggered by an osmotically induced increase in the cytoplasmic volume of the rod OS. We use these results to measure the hydraulic conductivity of the rod plasma membrane, to quantify osmolyte production by G-protein activation, to estimate a spring constant for previously reported molecular links between the rod disc membranes, and to quantitatively explain the backscattering from rods in terms of refractive index changes arising from OS swelling and light-stimulated translocation of G protein from the disc membranes.

Results

Photoactivation of Rhodopsin Increases Near-Infrared Backscattering from Rods and Causes Lengthening of Their OS. A brief 488-nm light exposure that photoactivated 10% of the rhodopsin in rod photoreceptors (Fig. 1*A*) produced dramatic changes in light backscattered from the posterior eye, as measured with near-infrared OCT (Fig. 1 *B* and *C*). Comparison of an OCT B-scan image taken in the dark-adapted state with one taken 2 min after the light exposure (Fig. 1 *B* and *C*) revealed large changes in backscattering in multiple retinal layers, and Movie S1 of the B

Significance

Complete activation of the phototransduction G-protein cascade of dark-adapted rod photoreceptors causes outer segments to undergo 10% elongation and large local increases in backscattering, as measured in vivo with noninvasive, high-resolution optical coherence tomography. Maximal elongation is caused by a potentially harmful 20% increase in internal osmotic pressure generated by excess osmolytes arising from phototransduction. The light-stimulated elongation and backscattering responses can be explained by an osmo-elastic model of cytoplasmic swelling, combined with changes in refractive index consequent to the swelling and translocation of the G-protein subunits into the cytosol. Disease conditions that affect the structural integrity of rods may cause them to be especially vulnerable to osmotic stress caused by bright light.

Author contributions: P.Z., R.J.Z., and E.N.P. designed research; P.Z. and M.G. performed research; R.J.Z., P.T.N., V.Y.-Y., and M.E.B. contributed new reagents/analytic tools; P.Z., R.J.Z., and E.N.P. analyzed data; P.T.N. and V.Y.-Y. performed molecular modeling; and P.Z., R.J.Z., M.E.B., and E.N.P. wrote the paper.

The authors declare no conflict of interest.

This article is a PNAS Direct Submission.

[1]To whom correspondence should be addressed. Email: enpugh@ucdavis.edu.

This article contains supporting information online at www.pnas.org/lookup/suppl/doi:10.1073/pnas.1620572114/-/DCSupplemental.

scans shows these effects to reach broad maxima around 2 min and subside toward baseline thereafter. To quantify these changes, we derived axial intensity profiles from the 5-min series of OCT scans (Fig. 1*D*). Inspection of the profile plots revealed a number of distinct phenomena that were reliably repeated in multiple experiments, including altered backscattering from (*i*) the external limiting membrane (ELM), (*ii*) the inner/outer segment (IS/OS) junction, (*iii*) the OS tip, (*iv*) Bruch's membrane (BrM) and (*v*) the sclera, and (*vi*) an increase in distance between the IS/OS junction and BrM and between the ELM and BrM.

To further analyze these phenomena we plotted their magnitudes as functions of time (Fig. 1 *E*, *F*, *H*, and *I*) and as covariates (Fig. 1 *G* and *J*). The time courses of the increases in backscattering from the IS/OS and OS tips were similar to each other (Fig. 1 *D*, *Inset*, and *E*) and similar to the time course of the anterior (leftward) shift of the IS/OS junction (Fig. 1*F*), suggesting that these physically distinct photoreceptor-layer effects were driven by a common mechanism. The leftward shift in the IS/OS peak has a distinctive linear rising phase, however, whereas the backscattering signals from the IS/OS and OS tips have a delayed, sigmoidal rise. Covariate analysis of these three photoreceptor-layer–specific signals confirmed their positive correlation, but underscored differences in their kinetics (Fig. 1*G*). Notably, whereas the ELM backscatter peak shifted toward the vitreous in lockstep with that of the IS/OS junction (Fig. 1*F*), the amplitude of the ELM backscatter changed very little (Fig. 1*I*). This suggests that elongation of the OS induces the IS to be displaced in tandem, while also revealing that backscattering from the ELM and IS/OS is caused by distinct mechanisms. [The OS tips appear to undergo a 0.3-μm displacement toward the vitreous. This is likely an artifact of the increased scattering by the tips (see *Effect of Limited OCT Axial Resolution on the Backscatter Profile of the Distal Rod OS* and Fig. S2).] In contrast to the backscattering from the IS/OS and OS tips, those from BrM and the sclera had biphasic kinetics, initially decreasing after the stimulus presentation and then returning toward baseline (Fig. 1*H*).

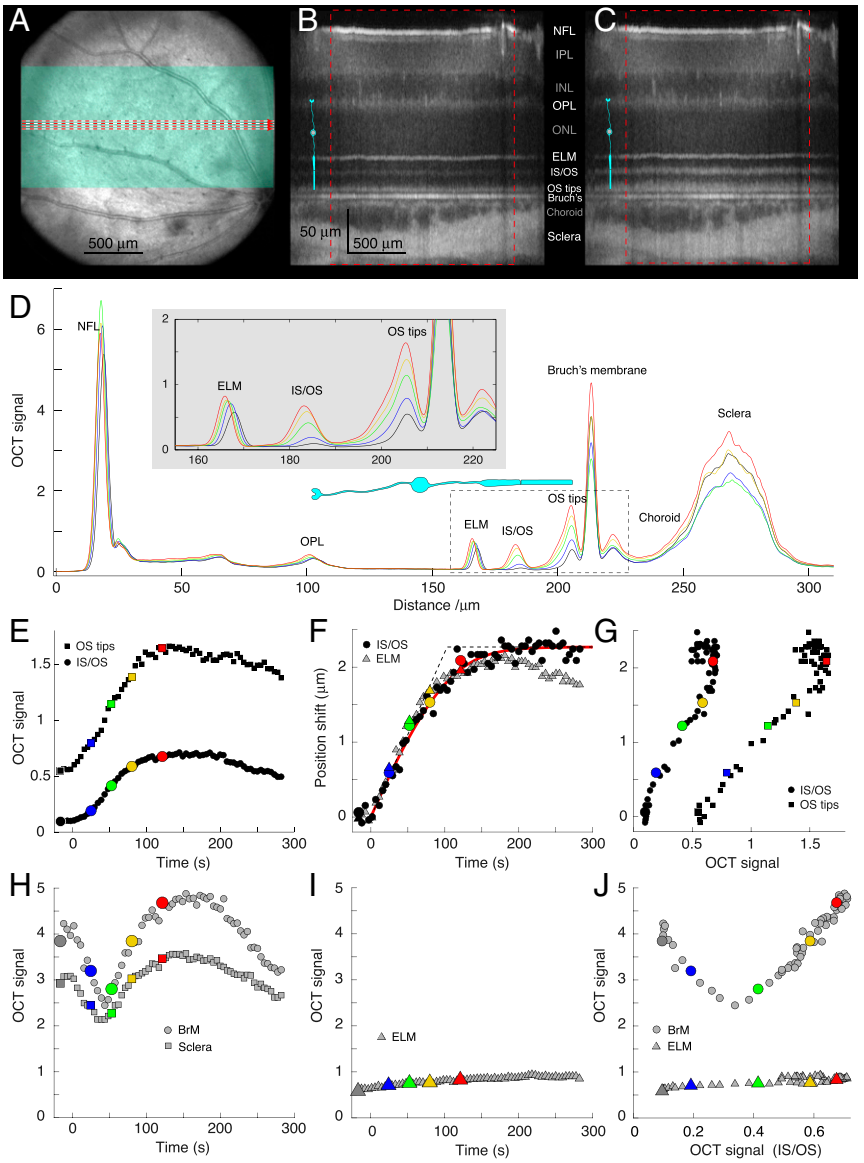

Fig. 1. Light stimulation triggers lengthening of rod OS and increased backscattering from the OS base and tips. (*A*) Light exposure and OCT scanning protocol. A blue-green rectangle representing the visual field to which 488 nm light was delivered with an SLO is superimposed upon an en face projection of an OCT scan of the retina of an albino (BALB/c) mouse; the single SLO scan took 0.92 s and isomerized 10% of the rhodopsin. OCT B scans at the positions of the four red dashed lines were taken every 0.92 s for 5 min. (*B* and *C*) OCT B scans taken before (*B*) and 2 min after (*C*) the 488-nm light exposure (the complete time series of B scans is provided in Movie S1). Retinal layer abbreviations are as follows: BrM, Bruch's membrane; ELM, external limiting membrane; INL, inner nuclear; IPL, inner plexiform; IS/OS, inner/outer segment junctions; NFL, neurofiber layer; ONL, outer nuclear; OPL, outer plexiform. The layer identifications are confirmed with histology in Fig. S1. (*D*) Axial backscattering profiles generated by averaging all of the OCT A scans (axial linescans) in the region identified by the red dashed rectangles in *B* and *C*. The profiles represent data collected in the dark before stimulation (black trace) and 25 s (blue), 52 s (green), 80 s (yellow), and 121 s (red) after delivery of the stimulus. A schematic rod (cyan) drawn to scale in *B*–*D* serves to localize key OCT features relative to rod anatomy. *D*, *Inset* (gray rectangle) shows an expanded view of the portion of the profiles circumscribed by the dashed rectangle. All A scans were aligned to the strong BrM reflectance before averaging. (*E*) The amplitude of the OCT backscattering from the base of the OS (IS/OS) and from the OS tip plotted as functions of time. The large colored symbols plot results extracted from the correspondingly colored traces in *D*, whereas the smaller solid black symbols were extracted from the other scans taken over the 5-min epoch. (*F*) The magnitude of the shift of the axial position of the center of the OCT bands arising from backscattering by the ELM and IS/OS plotted as a function of time. The dashed lines plot the initial slope and saturated level, respectively, whereas the red curve is generated with an osmo-elastic model described in the text. (*G*) The position shift of the IS/OS band plotted as a function of the amplitude of the OCT backscattering from the IS/OS and OS tips. (*H* and *I*) Magnitude of OCT backscattering signals from BrM, the sclera, and the ELM as a function of time. (*J*) BrM and ELM OCT signals plotted as covariates of IS/OS. [Here and throughout the paper, OCT signals are presented on a common scale: Thus "OCT signal" signifies $S^2_{OCT} \times 10^{-8}$, where S_{OCT} is the amplitude of the FD-OCT signal (*Materials and Methods*).] $S^2_{OCT}(z)$ is used because it is linearly proportional to the intensity of the light backscattered from depth z (*Materials and Methods*, Eqs. **5**–**7**). For clarity, the lateral (x)- and axial (y)-scale factors for the OCT B scans in Fig. 1 *B* and *C* are not equal (cf. Fig. S1). The data were obtained from a BALB/c (albino) mouse.

Plotting these latter signals as a function of the IS/OS backscatter signal (Fig. 1*J*) further highlighted the distinctive character of the scattering from the layers posterior to the photoreceptors and retinal pigment epithelium (RPE). Overall, these data and analyses reveal the various light-stimulated effects to be layer specific and distinctive in kinetics and clearly not a generic tissue response. The use of an albino BALB/c mouse, which lacks melanin pigmentation in the RPE and choroid, allowed the OCT beam to penetrate all of the way to the sclera, but closely similar results were obtained with pigmented (C57BL/6J) mice (Fig. 2 and Table 1).

Activation of the Rod G-Protein Transducin Is Necessary for the Elongation and Backscattering Changes of the Rod OS Layer. We tested the hypothesis that the increased backscattering and OS elongation are caused by activation of rod phototransduction by repeating the experiment of Fig. 1 in mice lacking $G\alpha_t$ (*Gnat1*$^{-/-}$). Although having normal ultrastructure and a full complement of rhodopsin, rod OS of *Gnat1*$^{-/-}$ mice do not transduce light into electrical signals (29). None of the light-stimulated changes observed in wild-type mice—with the exception of that from BrM—were observed in *Gnat1*$^{-/-}$ mice with either weak (Fig. 2*A*) or normal pigmentation (Fig. 2*B*). Pigmented C57BL/6J control mice exhibited changes very similar to those of albino mice (Fig. 2*C*), showing that whereas melanin screens backscatter from the rod tips and from BrM and deeper layers, its presence does not affect the OCT signals originating in layers anterior to the RPE (Table 1). These results establish that activation of $G\alpha_t$ by photoisomerized rhodopsin is necessary for production of the photoreceptor-layer–specific backscattering increases and for the concomitant increase in OS length.

Rhodopsin Bleaching Dependence, Kinetics, and Reversibility of the Backscattering Signals. To obtain further insight into the phototransduction-induced increases in rod OS backscattering and length, we measured the time courses of these effects in response to light varied in intensity over a 200-fold range (Fig. 3). Both effects were graded in amplitude and duration with stimulus strength (Fig. 3 *A*–*D*). Amplitude vs. intensity plots showed them to have similar dependence on the fraction of rhodopsin isomerized per rod (Fig. 3 *E* and *F*). The light sensitivity of these effects is far lower, however, than that of the rod electrical response. The mouse rod cGMP-activated current, when measured in vivo under identical conditions, is half-saturated by a flash producing ~100 photoactivated rhodopsins (R*) (30). In contrast, the OS elongation measured in our experiments was half-saturated by a stimulus that bleached ~2% of the rhodopsin and produces ~10^6 R* (Fig. 3*E*). These data strongly reject the hypothesis that the

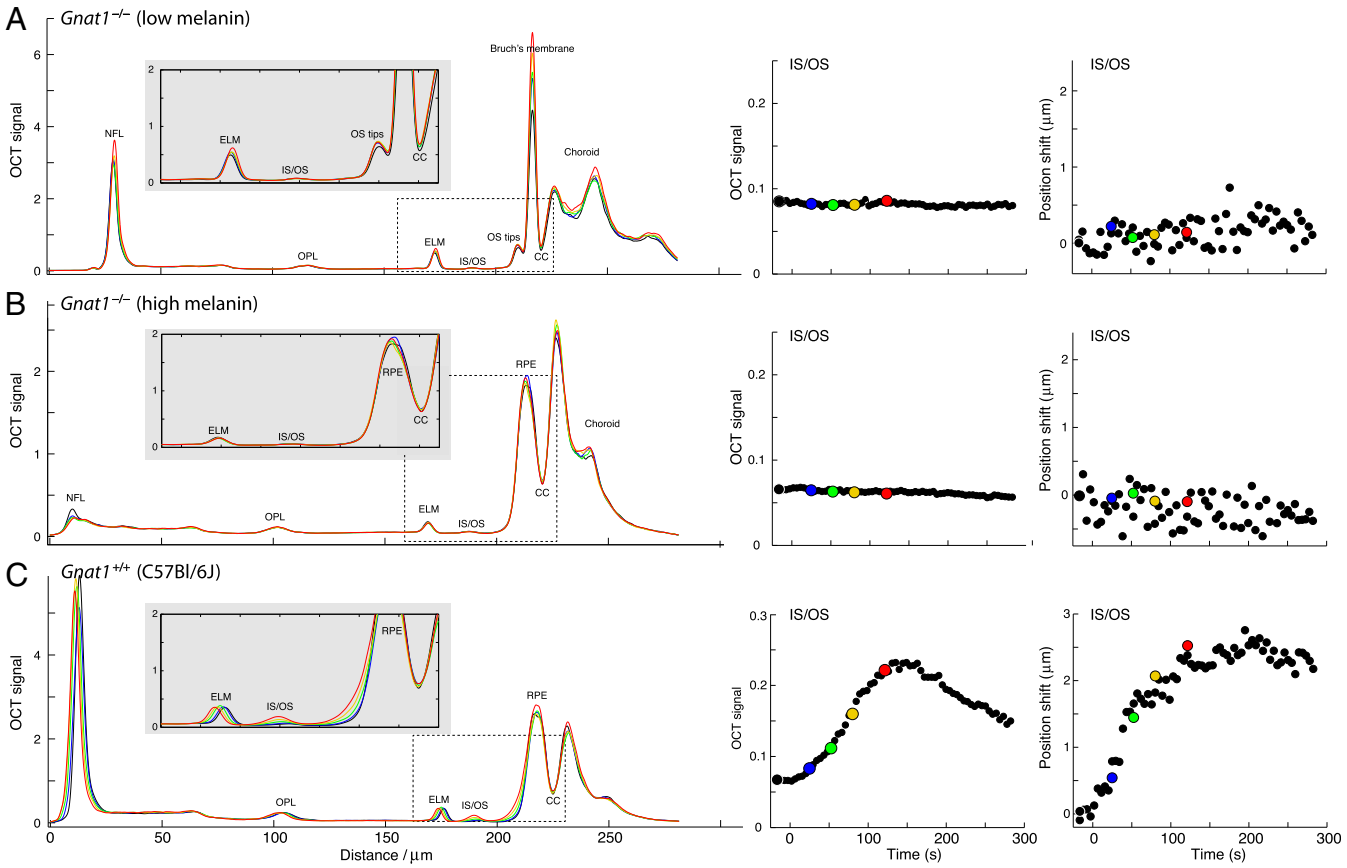

Fig. 2. OS elongation and increased backscattering are triggered by rhodopsin activation of the $G\alpha_t$. *A*–*C*, *Left* present OCT profiles obtained in experiments identical to that in Fig. 1, but with mice of different genotypes: *A* and *B* are from mice null for $G\alpha_t$ (*Gnat1*$^{-/-}$), but having relatively low (*A*) and relatively high (*B*) melanin expression; the dark-adapted OCT profiles of the low-melanin mouse in the posterior eye more closely resemble that of the albino mouse in Fig. 1, enabling both the IS/OS boundary and OS tips boundary to be seen. In pigmented mice (*B* and *C*) melanin backscattering from the RPE and choroid obscure the OS tips and BrM. However, in the pigmented mice the choriocapillaris "dip" (CC) in the profiles provided a sharply defined locus for alignment of the scans. Note that the profile data in *Insets* (gray boxes) are presented with identical *x* and *y* scaling. *A*–*C*, *Center* and *Right* present the amplitude of the backscatter from the IS/OS (*Center*) and the position shift of the IS/OS boundary (*Right*), respectively, extracted from the full set of profiles. The colored symbols correspond to the OCT profile scans at the time points indicated in Fig. 1 legend, whereas the solid black symbols were extracted from profiles not shown. The relatively high variability of the position shift data of the *Gnat1*$^{-/-}$ is due to the relatively small amplitude of the IS/OS backscatter amplitude.

Table 1. Features of rod osmotic swelling and backscatter increases measured with OCT

	Rod OS		Water influx into rod OS				Backscatter from IS/OS		
Strain, *N*	Length, μm	Increase, μm	Max. rate, $\mu m^3 \cdot s^{-1}$	Total, μm^3	L_P, $cm^3 \cdot s^{-1} \cdot dyn^{-1}$	P_f, $cm \cdot s^{-1}$	Dark, $S^2_{OCT} \times 10^{-8}$	Light, $S^2_{OCT} \times 10^{-8}$	Ratio
BALB/c, 11	19.3 ± 0.1	2.1 ± 0.1	0.033 ± 0.006	3.2 ± 0.2	$1.7 \pm 0.1 \times 10^{-14}$	2.3×10^{-5}	0.12 ± 0.01	0.55 ± 0.05	4.9 ± 0.5
C57Bl6/J, 7	21.1 ± 0.6	1.9 ± 0.2	0.032 ± 0.011	2.8 ± 0.2	$2.0 \pm 0.2 \times 10^{-14}$	2.8×10^{-5}	0.06 ± 0.01	0.22 ± 0.05	3.5 ± 0.4
Gnat1$^{-/-}$, 10	21.7 ± 1.3	0.007 ± 0.12	—	—	—	—	0.10 ± 0.02	0.08 ± 0.01	0.9 ± 0.1

The first row identifies features of mouse rod OS measured with OCT, the second row identifies measured parameters associated with the feature, and the third row gives the physical units of the latter (where appropriate). Numerical entries are mean ± SEM of data from the experimental paradigm illustrated in Fig. 1 (10% bleaching exposure). Length measurements assumed an average refractive index of 1.410 for the rod OS. Water influx parameters were estimated from fitting the osmo-elastic model (Eq. **1**) to rod OS elongation data (e.g., Fig. 1*F*, red trace), assuming the dark-adapted cytoplasmic volume is 56% of the rod OS envelope volume (Fig. 4 and *Osmo-Elastic Model of Light-Induced Rod OS Swelling*). For the rod OS diameter of 1.4 μm (61), the cytoplasmic volume of a 20-μm long, dark-adapted mouse rod OS is 17.2 μm^3. S^2_{OCT} specifies the backscatter power in instrumental units of the OCT. Hydraulic conductivity (L_P) and water permeability (P_f) were computed for each experiment with Eq. **2**, as described in the text.

elongation is triggered by the closure of the cGMP-gated (CNG) channels or attendant water transport via AQP4 channels in Müller cells, which swell in response to K^+ uptake (31). First, the rod OS swelling and backscattering increases are more than four orders of magnitude less sensitive to light than the closure of the CNG channels that underlies the rod's electrical response (Fig. 3 *E* and *F*). Second, the intense stimuli used here completely close the CNG channels in less than 1 s, and the consequent light-dependent K^+_o increase and uptake by Müller cells would be expected to have comparable light sensitivity and kinetics. In contrast, at its maximal rate elongation takes more than 100 s to reach its saturated amplitude (Fig. 1 *E* and *F* and Fig. 3 *A*–*D*). Third, the elongation is confined to the OS layer, defined by the backscattering from the OS tips and IS/OS junction (Fig. 1 and Fig. S1), layers of the retina in which Müller cells project only minimal apical processes. Fourth, recent work using a somewhat different stimulation paradigm has confirmed histologically that the mouse rod OS layer elongates under light conditions that give rise to elongation visualized with OCT (32).

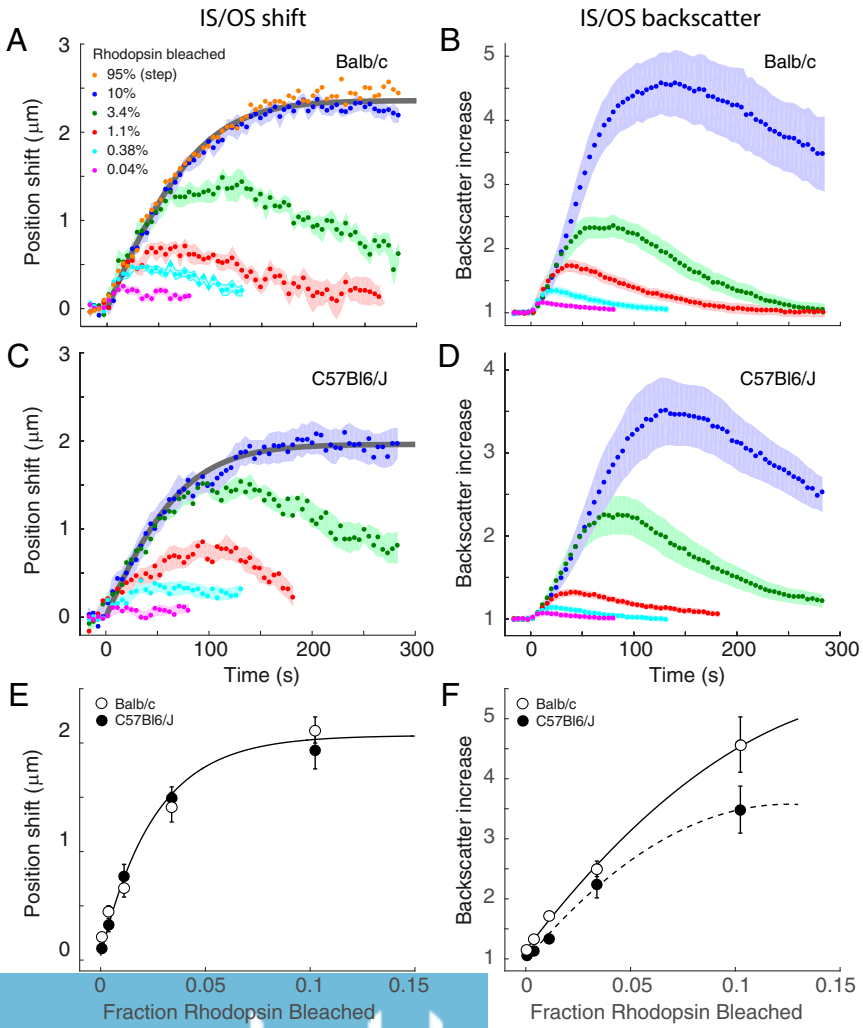

Fig. 3. Rhodopsin bleach dependence and kinetics of rod elongation and backscattering increases. Results were obtained with the experimental paradigm of Fig. 1, using both albino (BALB/c) mice (*A* and *B*) and pigmented (C57Bl6/J) mice (*C* and *D*) with light exposures that bleached between 0.04% and 95% of the rhodopsin (symbol key in *A*). *E* and *F* plot the dependence of the amplitudes of the elongation (*E*) and IS/OS backscatter increases as a function of the bleach level. The smooth curve in *E* is an exponential function that reaches 1-e^{-1} of the saturated level at a 2.6% level of bleaching; the smooth curves in *F* are quadratic functions that serve to highlight the declining rate of backscatter increase with increasing bleach level. In *A*–*D* the symbols plot mean values, and the colored backgrounds plot the SEMs of the traces. Each trace is the average of at least 6 experiments from both eyes of at least three mice. For the lower bleach levels up to 44 individual experiments were averaged. (OCT data collection was truncated short of 300 s in the experiments with the three lowest bleach levels.) The fraction bleached can be converted into photoisomerizations per rod (R*) by multiplying by 7×10^7, the average number of rhodopsin molecules per mouse rod (81).

The Molecular Mechanism of the Rod OS Elongation and Backscattering. We sought to explain the OS swelling and backscattering increases in terms of events associated with rhodopsin activation of $G\alpha_t$ (Fig. 4). As the increases in scattering imply a substantial redistribution of the molecular mass in the rod OS that underlies its unusually high refractive index of 1.41 (33) and previous in vitro investigations found light-scattering changes dependent on $G\alpha_t$ (34, 35), we focused on the role of $G\alpha_t$. Because the G-protein heterotrimer $G\alpha_t\beta_1\gamma_1$ is present in the dark-adapted rod OS at 1:8 relative to rhodopsin (36, 37) and has more than twice rhodopsin's mass per molecule, it comprises ∼20% of the total mass of transduction-associated proteins in the dark-adapted rod OS. In the dark-adapted state, inactive $G\alpha_t\beta_1\gamma_1$ is anchored to OS disc membranes by N-terminal myristoylation of $G\alpha_t$ and C-terminal farnesylation of $G\gamma_1$ (38). Activation of $G\alpha_t$ by light exposures that isomerize large fractions of rhodopsin causes the $G\alpha_t$ and $G\beta_1\gamma_1$ subunits to dissociate not only from one another, but also from the disc membrane, as established by translocation of $G\alpha_t$ and $G\beta_1\gamma_1$ to the IS in vivo in prolonged bright light (39). Because rod OSs behave as osmometers, swelling or shrinking when exposed to altered osmotic strength media (40, 41), we hypothesized that transduction reactions associated with complete activation of $G\alpha_t$ induce osmotic swelling and that the swelling, combined with mass redistribution of $G\alpha_t$ and $G\beta_1\gamma_1$ from the disc membranes into cytosol, might in turn underlie the scattering increases at the IS/OS and OS tips. We tested this hypothesis by developing a model that incorporates relevant facts about the mouse rod OS and comparing predictions of the model with our data.

Maximal Activation of Phototransduction Increases Rod OS Osmolarity by at Least 65 mOsM. In constructing a model for phototransduction-induced osmotic swelling of the rod OS, we first considered the consequences of water influx. As moderate osmotic perturbation alters only rod OS length and not width (40, 41), length increases can be readily converted into volume changes and influx rates. The swelling response showed a light dependence consistent with maximal activation of $G\alpha_t$, reaching a saturated amplitude in response to light that isomerizes ∼1 R* per $G\alpha_t$ (Figs. 1*F* and 3 *A* and *C*). Because the disc membranes occupy ∼50% of the OS volume (Fig. 4 *B* and *C*), the saturated 10% elongation corresponds to an ∼20% increase in cytoplasmic volume (Fig. 4*D*). Assuming the saturated swelling is a purely osmotic equilibrium, Van't Hoff's law dictates that the fractional volume increase is proportional to the incremental osmotic pressure; i.e.,

$$\Delta V_{cyto}/V_{cyto,rest} = \Delta\Pi/\Pi_{rest}, \quad [1]$$

where Π_{rest} is the resting (dark-adapted) osmotic pressure, and $\Delta\Pi = [\Delta n_S/V_{cyto,rest}]RT$ is the incremental osmotic pressure generated by Δn_S mol of novel osmolyte released into the cytoplasmic volume $V_{cyto,rest}$. Because Π_{rest}/RT = 325 mOsM is normal rodent plasma osmolarity (42), the 20% cytoplasmic volume increase implies the surprising result that maximal activation of phototransduction increases the rod OS cytoplasmic osmolarity by $\Delta n_S/V_{cyto,rest}$ = 65 mOsM. This value must be considered a lower limit, however, because the rod OS may possess an elastic mechanism to resist swelling, as we shortly examine.

The Hydraulic Conductivity of the Rod OS Membrane Is Consistent with That of a Membrane Lacking Aquaporin Channels. Our results also determine an upper limit for the water permeability of the rod OS plasma membrane. Water inflow (J_{H_2O}) should obey an osmo-elastic relation (43–45)

$$J_{H_2O} = L_P S_{ROS}(\Delta\Pi - P), \quad [2]$$

where L_p is hydraulic conductivity, S_{ROS} is the surface area of the rod OS, and P is the pressure from an elastic restoring force (cf. Eq. S1). Eq. **2** can be reformulated as a rate equation for the incremental cytoplasmic volume ΔV_{cyto}, whose solution predicts the time course of the light-stimulated rod OS (represented by ROS) volume increase (Fig. 1*F*, red curve; Fig. 3 *A* and *C*, gray curves; and *Osmo-Elastic Model of Light-Induced Rod OS Swelling* and Fig. S3). The initial slope (Fig. 1*F*, dashed line) multiplied by the rod OS cross-section (1.54 μm^2) yields the maximal water influx, whose average value is 0.03 μm^3·s^{-1} (Table 1). Applying Eq. **2** with S_{ROS} = 110 μm^2 and P = 0, we thus find $L_P = 1.6 \times 10^{-2}$ μm^3·s^{-1}·dyn^{-1}, corresponding to a water permeability coefficient $P_f = (RT/V_W) \times L_P = 2.3 \times 10^{-5}$ cm·s^{-1} (V_W = 18.2 cm^3·mol^{-1}). This estimate of P_f is notably lower than that measured by Preston et al. (46) for oocytes at 25 °C not expressing aquaporin channels (2.6×10^{-3} cm·s^{-1}), but closer to that (2.0×10^{-4} cm·s^{-1}) measured by Prescott and Zeuthen (47) in the same preparation.

Estimating the Spring Constant of an Elementary Rod OS Elastic Element. Freeze-fracture and cryoelectron tomographic investigations have revealed macromolecular structures that appear to link adjacent disc membranes (48, 49). Because most proteins can act as elastic elements (50), it is reasonable to hypothesize that such disc-to-disc "linkers" serve as springs that resist swelling, affording some protection of the rod OS from stimulus-induced osmotic overload. As rod OSs primarily swell axially in response to osmotic challenge (40, 41), if the OS has an elastic response, the steady-state elongation should obey Hookes' law

$$(\Delta\Pi_0 - \Delta\Pi_{min})A_{ROS} = k_H \Delta L(\infty), \quad [3]$$

where $\Delta\Pi_0/RT$ is the increment in osmolarity, $\Delta\Pi_{min}/RT$ = 65 mOsM is the minimum increment compatible with the data, A_{ROS} is the rod OS cross-section, k_H is the spring constant, and $\Delta L(\infty)$ is the steady-state length increase. For example, for $\Delta\Pi_0/RT$ = 75 mOsM, k_H = 12 dyn·cm^{-1} (12 pN·nm^{-1}). Because molecular springs between individual pairs of discs will act in parallel to oppose osmotic swelling, while the discs are in series, the overall spring constant of the rod OS is related to the molecular spring constant $k_{molecular}$ by

$$k_H = \frac{k_{molecular}\,\rho A_{ROS}}{N_{disc} - 1}. \quad [4]$$

Here ρ is the spatial density of the spring-like molecules, A_{ROS} is the surface area of a disc, and N_{disc} is the total number of discs. Nickell et al. (49) report a disc "spacer" density ρ = 492 μm^{-2}, and so given 625 discs in the 20-μm–length rod OS of this study, the elementary elastic unit is estimated to have a spring constant of $k_{molecular}$ = 15 pN·nm^{-1}. This is well within the range of the spring constants for proteins from single-molecule methods in the nondenaturing range of stretch (50, 51). More generally, our experiments provide a means of testing hypotheses about the identity of any component of the rod OS that could act as a molecular spring. An interesting candidate is the cGMP phosphodiesterase, which may span the interdiscal space (Fig. 4 *C* and *D*) and is present at 1:310 relative to rhodopsin (52), so that it has a surface density on pairs of discs of 250 μm^{-2}, intriguingly close to that of the as-yet unidentified "spacers" (49).

An elastic response by the rod OS disc stack is not the only mechanism by which the rod could protect itself from phototransduction-induced osmotic stress. Another mechanism is the active or passive (diffusional) redistribution of excess osmolytes between segments. Diffusional redistribution driven by concentration gradients will very likely occur and, if so, would contribute to underestimation of the osmotic stimulus. One well-studied light-stimulated redistribution from the OS to the IS is that of $G\alpha_t$ and $G\beta_1\gamma_1$ (20, 39, 53). In this case, however, the total quantity of osmolyte (∼1.5 mM) and the maximum rate of redistribution (∼0.002 s^{-1}) (39) appear too small to materially affect the rod OS elongation measured here.

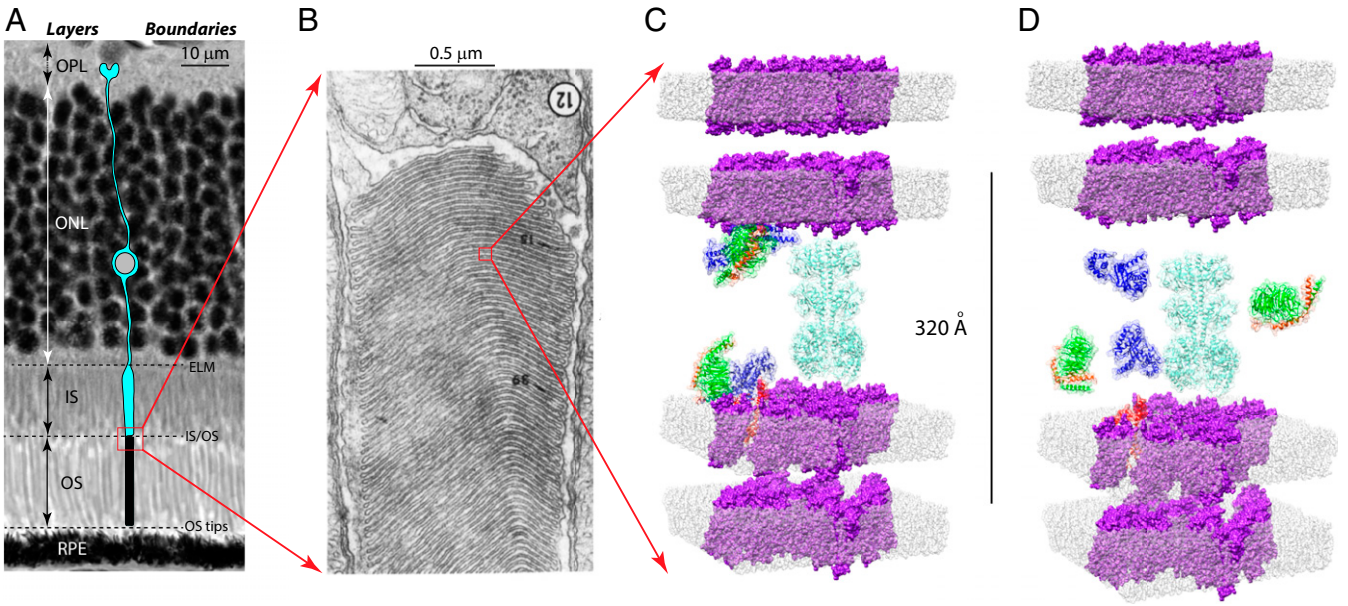

Fig. 4. Cellular and molecular elements underlying rod osmotic swelling. (*A*) Rod schematic (cyan) overlaid on a micrograph of a plastic section of a mouse retina. (*B*) Electron micrograph of the base of a mouse rod OS from the classic study of Carter-Dawson and LaVail, reprinted with permission from ref. 61. (*C*) Structural model of 20-nm × 20-nm patches of two pairs of adjacent disc bilayers in a dark-adapted rod OS, identified in *B*. Illustrated are rhodopsins (purple, eight per patch, corresponding to 25,000 μm^{-2}), two heterotrimers ($G\alpha_t$, blue; $G\beta_1$ green; $G\gamma_1$, red), and one phosphodiesterase (cyan). The disc-to-disc spacing was set to 32 nm (*Materials and Methods*). (*D*) Molecular-scale consequences of osmotic swelling: The interdiscal cytoplasmic space is stretched by ~20%, and the G-protein heterotrimers are dissociated into $G\alpha_t$ and $G\beta_1\gamma_1$ components and solubilized. ELM, external limiting membrane; ONL, outer nuclear; OPL, outer plexiform.

Nonetheless, the initial step in this redistribution—dissociation of $G\alpha_t$ and $G\beta_1\gamma_1$ from the disk membranes—may contribute to increased backscattering, as now discussed.

The Increased Backscattering from the Base and Tips of Rods Arises from Light-Induced G-Osmotic Swelling and G-Protein Translocation. It has long been known that light-stimulated translocation of $G\alpha_t$ and $G\beta_1\gamma_1$ into the aqueous phase can produce scattering changes in vitro in suspensions of disc membranes or permeabilized rod OSs (17, 35, 54), and so we investigated whether similar translocation from the disk membrane into swollen cytosol could give rise to increased scattering at the rod OS base and tips. Backscattering occurs at retinal layer boundaries where forward-propagating light encounters a change in refractive index. The average refractive indexes of the IS and OS of rods have been measured to be $\bar{n}_{IS} = 1.40$ and $\bar{n}_{OS} = 1.41$ (33). These exceptionally high refractive indexes, which arise from dense concentration of proteins and lipids, enable photoreceptors to act as dielectric wave guides, trapping and condensing light in the IS and guiding it into the OS (28, 55–57).

We considered two hypotheses as explanations of the increased rod OS backscattering: (*i*) Solubilization of $G\alpha_t$ and $G\beta_1\gamma_1$ combined with osmotic swelling causes the refractive index of the rod OS to change uniformly relative to those of the IS and of the extracellular space and RPE cells surrounding the OS tip (8) and (*ii*) solubilization of $G\alpha_t$ and $G\beta_1\gamma_1$ combined with osmotic swelling causes the index of refraction at the base and tip of the OS to decrease relative to that of the remainder of the OS. Hypothesis *i* was rejected, as follows. In the dark-adapted rod the exceptionally high refractive indexes of the IS and OS (33) certainly exceed those of the extracellular matrix and RPE near the OS tips. Calculations based on well-known dielectric mixing models (58–60) predict that 10% elongation of the rod OS will cause the average refractive index of the OS to decrease (*Model of the Light-Induced Backscatter Increase from the OS* and Fig. S4). As a consequence, the refractive index differentials between the IS and the OS, and between the OS tip and the adjacent media, are both predicted by hypothesis *i* to decrease, leading to decreased rather than to increased backscattering as is observed.

The alternative hypothesis (*ii*) rests on the fact that a number of basal discs (and possibly distal discs) of the rod OS are not closed and internalized in the OS, but rather like classic cone discs are contiguous with the plasma membrane (61, 62) (Fig. 5). As a consequence osmotically driven water influx through non-internalized basal discs will be substantially increased relative to that of the rest of the rod OS. We combined this insight with a three-layer model of the refractive index of the OS (59) and a model of the rod OS base (Fig. 5 *A* and *B*) and found that the resultant model (*Estimation of the Absolute Retinal Reflectivity Measured by the OCT System*, Fig. S5, and Tables S1 and S2) could predict the time course of increased backscattering (Fig. 5*F*). Although the model is not unique and will certainly undergo further tests and refinement, it nonetheless serves as a proof of principle, namely that a combination of osmotic and electromagnetic theory can provide a simultaneous account of the correlated but physically distinct rod OS swelling and backscattering increases.

Discussion

Our results establish that mouse rod OSs elongate and undergo increased backscattering from their base and tip when stimulated with light that strongly activates rod phototransduction (Figs. 1–3).

Rod OS Elongation Is Caused by G-Protein–Induced Osmotic Swelling. Previous investigations have reported light-induced changes in the length of photoreceptor OSs measured in vivo (32), including recently from human cone OSs (10). Three lines of evidence presented in this work support the hypothesis that the elongation reported here results from osmotically induced swelling triggered by excess osmolytes generated by phototransduction reactions at or downstream of $G\alpha_t$ activation. First, the swelling response is absent in mice lacking $G\alpha_t$ expression (*Gnat1*$^{-/-}$; Fig. 2). Second,

the magnitude of the swelling response is saturated by stimuli that produce ~1R* per $G\alpha_t$ and so clearly maximally activates phototransduction (Fig. 3). These two lines of evidence reject the hypothesis that activation of rhodopsin per se or production of retinoid byproducts drives the swelling, as *Gnat1*$^{-/-}$ mice have normal OSs and rhodopsin (29), and a 100% bleaching stimulus causes no more swelling than a 10% bleach in normal mice (Fig. 3*A*). Third, the elongation data yield an estimate of the rod OS H_2O permeability that is reasonable for a membrane lacking aquaporin (46). The estimate of the minimal osmotic increment (20%; 65 mOsM) underlying the maximal swelling is unexpectedly large and must be even larger if swelling is resisted by spring-like links between the disc membranes (49) or osmolyte diffusion between ISs and OSs.

Phototransduction-Generated Osmotic Stress and Mechanisms of Protection. Our work shows that the exposure of the dark-adapted eye to light that isomerizes only 10% of the rhodopsin produces an ineluctable osmotic stress in rods, the most numerous cell in the retina. Red blood cells (RBCs) have mechanisms that allow them to cope with osmotic stress such as encountered in their passage through the kidney. Nonetheless, standard osmotic fragility assays show that ~50% of normal RBCs rupture in a 45% hypo-osmotic medium, whereas abnormal RBCs are disrupted by substantially lower osmolarity decreases (e.g., refs. 63 and 64). Translocation of dissociated $G\alpha_t$ and $G\beta_1\gamma_1$ off the disc membrane and to the IS (20, 39) will reduce potentially dangerous osmotic stress caused from stimuli that bleach large fractions of rhodopsin. The retinas of individuals with hereditary or other disease conditions

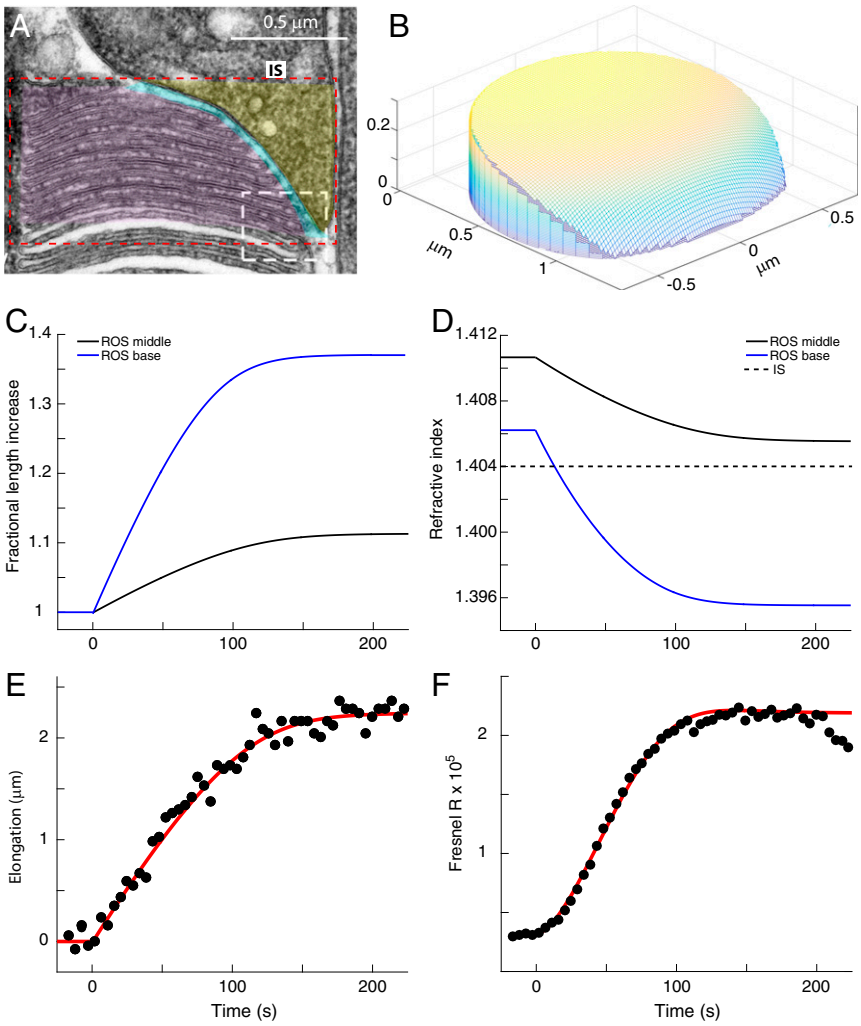

Fig. 5. Modeling of the light-induced backscattering increase from the base of the rod OS. (*A*) Electron micrograph of the base of a mouse rod OS from the recent study of Ding et al. (62). Reprinted with permission from Vadim Arshavsky (Duke University, Durham, NC). The "rod OS base" as defined for the backscattering model (red dashed region) is a cylindrical portion of the rod comprising three elements: the IS component (colored yellow); the OS component, comprising eight basal discs in various stages of assembly (pale purple); and the intervening extracellular space (cyan). In this instance, Ding et al. showed that eight basal disc membranes remain fused with the plasma membrane and would thus contribute to an elevated water permeability of the rod OS base. (*B*) Depiction of a 3D model of the rod OS component of the base (i.e., portion of based disc composed of nascent discs). A dielectric mixing model was developed that combines the predicted time-varying refractive index of the basal discs dictated by osmotically induced swelling, and $G\alpha_t$ and $G\beta_1\gamma_1$ dissociation and solubilization, with portions of the rod OS base that are IS (yellow) or extracellular (cyan). (*Model of the Light-Induced Backscatter Increase from the OS*). (*C*) Fractional increases in the length of the main ("middle") portion of the rod OS and the basal discs predicted by the model. (*D*) Changes in the refractive indexes of the basal and middle portions of the rod OS predicted by the model along with the unchanging refractive index of the rod IS. (*E*) Rod OS swelling data from Fig. 1*F* (solid black circles), with prediction of the osmo-elastic model (red curve). (*F*) "IS/OS" (rod OS base) backscatter data (solid black circles) adjusted from the measured value of S^2_{OCT} converted to equivalent Fresnel reflectivity compared with the model prediction (red curve) (*Estimation of the Absolute Retinal Reflectivity Measured by the OCT System*).

that impair the structural integrity of rods, however, may have elevated light-damage susceptibility arising from an inability to cope normally with transduction-induced osmotic stress.

Explaining Transduction-Induced Backscattering from the Base of the OS. Previous studies have reported light-stimulated increases in backscattering from the photoreceptor layer of the retina in vivo (8, 9, 12, 14). OCT enables the retinal layer of these light-stimulated "intrinsic optical signals" to be precisely determined, and we have focused on those arising from the OS layer (Figs. 1–3). We hypothesize that these intrinsic signals arise from changes in the local refractive index in the rod OS caused by osmotically induced cytoplasmic swelling and translocation of $G\alpha_t$ and $G\beta_1\gamma_1$ into the cytosol (Fig. 4). A key finding of our study is that OS elongation and increased backscattering at the IS/OS boundary—despite arising from physically distinct processes—are interlinked by their kinetics and light dependence, i.e., the degree of stimulation of the phototransduction cascade (Figs. 1–3). Moreover, our analysis has shown that the magnitude and kinetics of these distinct but concurrent processes can be explained by a framework incorporating an osmo-elastic rod OS response and a physical model of the backscattering process (Fig. 5 and *Model of the Light-Induced Backscatter Increase from the OS*).

Activation and Deactivation of Phototransduction After Strong Bleaching of Rhodopsin. Because a single fully active rhodopsin (R*) is capable of activating hundreds of G proteins per second (34, 65), it may seem surprising that a 10% bleaching exposure, which produces R* equimolar to $G\alpha_t\beta_1\gamma_1$, is required for maximal rod OS elongation (Fig. 3). Distinguishing between rate and amplitude saturation in the context of the osmo-elastic model of elongation helps resolve this puzzle. Rate saturation—the maximal rate of OS length increase—in the model is reached when complete activation of phototransduction produces the maximum possible osmotic stimulus. In contrast, amplitude saturation in reached only when the very slow water entry brings the OS into osmotic equilibrium. Because the rate of elongation reaches its maximal value after exposure to stimuli that bleach 0.38% or less rhodopsin (Fig. 3 *A* and *C*), our analysis implies that at least 26 $G\alpha_t$s are activated per R* at the lowest bleach levels used in our experiments.

Dark adaptation after strong bleaching of rhodopsin has been traditionally investigated in vivo with psychophysical and electrophysiological methods (reviewed in ref. 66). These methods can be used only at times when phototransduction activity has decayed to the extent that at least some CNG channels are open and capable of being closed in response to subsequently delivered light stimuli used to measure sensitivity. The OCT methodology used here is not limited to conditions when CNG channels are open and affords the possibility of investigating deactivation of phototransduction in vivo in heretofore unexplored conditions. Indeed, the OCT elongation and backscattering signals clearly exhibit substantial "turnoff" over 5 min after exposures that bleach up to 10% of the rhodopsin (Fig. 3 *A–D*), suggesting that G-protein deactivation and reassociation with the disc membranes is occurring. This deactivation in turn implies that R* activity is decreasing over this time window, for otherwise repeated activation of G protein would presumably keep the G protein dissociated. It is unlikely that rhodopsin regeneration contributes to the inferred decline in R* activity, because the maximal rates of regeneration in BALB/c and C56Bl6/J mice differ by threefold [2.2% min^{-1} and 0.7% min^{-1}, respectively (67)], whereas the recoveries of the OCT signals in the two strains are closely comparable (Fig. 3 *A–D*), and moreover even at the faster rate only 11% of the initially bleached rhodopsin would be regenerated. An alternative explanation is that activated rhodopsin molecules, which at such high bleach levels likely overwhelm deactivation by rhodopsin kinase and arrestin, are undergoing spontaneous decay. Notably, spontaneous decay of metarhodopsin II in mouse rods has a time constant of ~40 s (68–70), comparable to the time course of the decline of OCT signals observed here.

Limitations of the Experimental Protocol. Our results are necessarily limited by the sampling rate (1.1 Hz) of our OCT B-scan sampling protocol and by issues such as the physical stability of the mouse eye and the long-term clarity of its ocular media. The relatively low sampling rate may miss important intrinsic optical signals that occur on faster timescales, especially immediately after light stimulation. Improvements in methodology including the use of adaptive optics should allow characterization with nonstimulating OCT of mouse retinal intrinsic optical signals that occur on both shorter and longer timescales than used here.

Intrinsic Optical Signals from Human Cones and Rods. As noted in the Introduction, intrinsic optical signals from individual human cone photoreceptors have been measured by a number of groups (10–14). The advanced state of adaptive-optics OCT methodology for the human eye enables such cone-specific intrinsic optical signals to be characterized with great precision and sensitivity, and rapid advances in measurement and clinical applicability of human photoreceptor optophysiology can certainly be expected (71). It remains to be seen whether elongation and backscattering increases in human cones and rods can be understood with the principles applied here to mouse rods. The fact that human cones can escape from electrical saturation in the presence of steady lights that bleach upward of 90% of their visual pigment (72), whereas rods are driven into electrical saturation by far less intense light, reveals that cones possess adaptational mechanisms that efficiently reduce the gain of phototransduction at high bleach levels and presumably also reduce the production and the effect of excess osmolytes. Moreover, cone OSs whose disc membranes are contiguous with the plasma membrane also have much greater surface/volume ratios than rods and likely also use ionic transport mechanisms to counter the osmotic stress of excess osmolytes produced by phototransduction.

Materials and Methods

Animals. All mouse husbandry and handling were in accord with protocols approved by the University of California Animal Care and Use Committee, which strictly adheres to all NIH guidelines and satisfies the Association for Research in Vision and Ophthalmology guidelines for animal use. Young adult pigmented C57BL/6J and albino BALB/c mice were obtained from Jackson Laboratories at age 2 mo and maintained on a 12:12, ~100-lux light cycle. The *Gnat1*$^{-/-}$ line was maintained in the laboratory and genotyped with standard protocols as previously described (29). Although lacking $G\alpha_t$ expression, rods of *Gnat1*$^{-/-}$ mice have a full complement of rhodopsin, which bleaches normally (29). Mice used for experiments were 3–6 mo of age. Anesthesia and imaging protocols are provided in ref. 28. Pupils were fully dilated to a diameter >2 mm with tropicamide and phenylephrine before experiments, as previously described (28), obviating vignetting of the ~0.5-mm OCT and SLO beams as they entered the eye. In addition, the conjugate aperture for the fiber-optic launch of the OCT sample arm light collector was much smaller than the dilated pupil, further ensuring that the OCT system's backscatter intensities were precisely calibrated.

Optical System and OCT Calibration. The combined SLO/Fourier-domain (FD)-OCT imaging system and calibration of the OCT depth scale, retinal scan area, and rhodopsin bleaching are described in detail in ref. 28. The superluminescent diode that served as the OCT light source has a 132-nm band (FWHM) centered on 860 nm and delivered 600 μW at the mouse pupil plane. Although OCT data are usually presented in a logarithmic (decibel) scale, we instead used a linear scale to more readily analyze the backscatter signals and compare them with predictions of reflectivity changes. We now provide a brief explanation of the FD-OCT signal intensity scaling. Thorough analysis of the signals in FD-OCT has been presented (e.g., refs. 73 and 74).

Adopting the notation of Fercher et al. (ref. 73, equation 4.19), the Fourier transform of the signal spectrogram satisfies

$$FT\{I(K)\} \propto ACF_F(z), \quad [5]$$

where $K = 2\pi/\lambda$ is the free-space wavenumber, $I(K)$ is the spectral density (proportional to intensity) as a function of K, z is the conjugate space coordinate of the sample, $ACF_F(z)$ is the autocorrelation function, and "$\propto$" signifies proportionality. For a delta-like reflectivity of magnitude R at sample position z_R, the backscattering potential is given by $F(z) = F_S(z) + \sqrt{R}\,\delta(z - z_R)$, and (neglecting small terms) the autocorrelation is

$$ACF_F(z) = \sqrt{R} F_S(z_R + z) \quad [6]$$

(ref. 73, equation 4.20). Thus, for a signal proportional to the local axial reflectivity $R(z)$ we used

$$S^2_{OCT}(z) \propto [ACF_F(z)]^2, \quad [7]$$

where S_{OCT} corresponds to the "raw" 16-bit FD-OCT signal. To estimate the proportionality factor in Eq. **7**, we performed an absolute calibration of the apparent sample reflectivity, using a mirror attenuated by neutral density filters as a delta-like reflectivity (*Estimation of the Absolute Retinal Reflectivity Measured by the OCT System* and Fig. S5).

Data Collection, Processing, and Analysis. The protocol used in the present experiments for OCT data collection and photobleaching is described in the context of Fig. 1. Each 0.92-s cycle of OCT scanning collected 4 closely spaced B scans comprising 512 A scans in the center of a 51° field of view (FOV). The 4 B scans were aligned with Matlab cross-correlation ("xcorr"), and A scans from the central 35° FOV segmented and aligned axially with the BrM peak (Balb/c) or with the choriocapillaris "dip" (C57Bl6/J). Average A-scan profiles (e.g., Fig. 1*D*) were obtained by averaging the aligned A scans from five successive cycles (4.6 s).

A-scan profiles were analyzed for their OCT signals at specific times and axial locations (with respect to BrM or RPE reference). Averaging across experiments was performed only on these extracted signals, and points were plotted as mean ± SEM (Fig. 3). Theoretical curves were fitted to data by least-squares methods with custom Matlab software, as described below and in *Model of the Light-Induced Backscatter Increase from the OS*.

Structural Model of the Rod OS. CHARMM-GUI (75, 76) was used to assemble an all-atoms model of 20-nm × 20-nm patches of disc membrane around 10 randomly spaced and randomly oriented rhodopsins [Protein Data Bank (PDB) ID 2I36] with transmembrane orientation based on prediction from the Orientations of Proteins in Membranes database (77). Lipids (PC, PE, PS, and cholesterol) were distributed in the inner and outer membrane leaflets according to results from bovine rod OS (78, 79). The spacings between the bilayer pair comprising an individual disc and between the pair of discs in the model were set for the dark-adapted state as described in *Model of the Light-Induced Backscatter Increase from the OS* and Fig. S4. $G\alpha_t\beta_1\gamma_1$ in its inactive heterotrimeric state (1GOT) docked to rhodopsin (3SN6) and dissociated subunits $G\alpha_t$ (1TND) and $G\beta_1\gamma$ (1TBG) and PDE6 (3IBJ) were added as required. The volumes of heterotrimeric $G\alpha_t\beta_1\gamma_1$ and its subunits were computed with Chimera (80).

Theoretical Models of Rod OS Osmotically Induced Swelling and Backscattering Increases. A model of bleaching-induced rod OS osmotic swelling was developed based on well-established physical and physiological principles (*Osmo-Elastic Model of Light-Induced Rod OS Swelling*) and tested by fitting the model to data to extract key features and parameters such as hydraulic conductivity. A model of the backscattering increases at the base of the rod OS was created by analysis of the refractive index distribution of the OS and of how this is affected by light-induced cytoplasmic swelling and the dissociation of $G\alpha_t$ and $G_t\beta\gamma$ from the disc membranes (*Model of the Light-Induced Backscatter Increase from the OS*). The backscattering model includes the osmo-elastic model and the simultaneous acquired swelling and backscattering data were fitted simultaneously (*Osmo-Elastic Model of Light-Induced Rod OS Swelling* and *Model of the Light-Induced Backscatter Increase from the OS*).

ACKNOWLEDGMENTS. We thank Prof. Roy Curry [University of California, Davis (UC Davis)] and Prof. Nader Engheta (University of Pennsylvania) for helpful comments on the osmo-elastic and backscattering modeling, respectively; Gabriel Peinado for help with characterization of the *Gnat1*$^{-/-}$ mice; and Dr. Sarah Karlen for assistance with mouse anesthesia and colony management. This research was supported by National Institutes of Health Grant EY02660 (to E.N.P.), a National Science Foundation Industry–University Cooperative Research Centers Program, Center for Biophotonic Sensors and Systems grant (to R.J.Z.), Grant EY012576 (National Eye Institute UC Davis core grant), and a UC Davis Research Investments in Science and Engineering (RISE) grant.

1. Drexler WF, Fujimoto JG, eds (2015) *Optical Coherence Tomography* (Springer, New York).
2. Fujimoto J, Huang D (2016) Foreword: 25 years of optical coherence tomography. *Invest Ophthalmol Vis Sci* 57(9):OCTi–OCTii.
3. Gao SS, et al. (2016) Optical coherence tomography angiography. *Invest Ophthalmol Vis Sci* 57(9):OCT27–OCT36.
4. Jang IK, et al. (2005) In vivo characterization of coronary atherosclerotic plaque by use of optical coherence tomography. *Circulation* 111(12):1551–1555.
5. Gonzalo N, et al. (2010) Second-generation optical coherence tomography in clinical practice. High-speed data acquisition is highly reproducible in patients undergoing percutaneous coronary intervention. *Rev Esp Cardiol* 63(8):893–903.
6. Li X, et al. (2005) High-resolution optical coherence tomographic imaging of osteoarthritic cartilage during open knee surgery. *Arthritis Res Ther* 7(2):R318–R323.
7. Fujimoto JG, Pitris C, Boppart SA, Brezinski ME (2000) Optical coherence tomography: An emerging technology for biomedical imaging and optical biopsy. *Neoplasia* 2(1-2):9–25.
8. Srinivasan VJ, Wojtkowski M, Fujimoto JG, Duker JS (2006) In vivo measurement of retinal physiology with high-speed ultrahigh-resolution optical coherence tomography. *Opt Lett* 31(15):2308–2310.
9. Yao X, Wang B (2015) Intrinsic optical signal imaging of retinal physiology: A review. *J Biomed Opt* 20(9):090901.
10. Hillmann D, et al. (2016) In vivo optical imaging of physiological responses to photostimulation in human photoreceptors. *Proc Natl Acad Sci USA* 113(46):13138–13143.
11. Jonnal RS, et al. (2007) In vivo functional imaging of human cone photoreceptors. *Opt Express* 15(24):16141–16160.
12. Grieve K, Roorda A (2008) Intrinsic signals from human cone photoreceptors. *Invest Ophthalmol Vis Sci* 49(2):713–719.
13. Kocaoglu OPL, et al. (2016) Photoreceptor disc shedding in the living human eye. *Biomed Opt Express* 7(11):4554–4568.
14. Schmoll T, Kolbitsch C, Leitgeb RA (2010) In vivo functional retinal optical coherence tomography. *J Biomed Opt* 15(4):041513.
15. Liu Q, et al. (2007) The proteome of the mouse photoreceptor sensory cilium complex. *Mol Cell Proteomics* 6(8):1299–1317.
16. Skiba NP, et al. (2013) Proteomic identification of unique photoreceptor disc components reveals the presence of PRCD, a protein linked to retinal degeneration. *J Proteome Res* 12(6):3010–3018.
17. Arshavsky VY, Lamb TD, Pugh EN, Jr (2002) G proteins and phototransduction. *Annu Rev Physiol* 64:153–187.
18. Arshavsky VY, Burns ME (2012) Photoreceptor signaling: Supporting vision across a wide range of light intensities. *J Biol Chem* 287(3):1620–1626.
19. Arshavsky VY, Wensel TG (2013) Timing is everything: GTPase regulation in phototransduction. *Invest Ophthalmol Vis Sci* 54(12):7725–7733.
20. Calvert PD, Strissel KJ, Schiesser WE, Pugh EN, Jr, Arshavsky VY (2006) Light-driven translocation of signaling proteins in vertebrate photoreceptors. *Trends Cell Biol* 16(11):560–568.
21. Kerov V, et al. (2005) Transducin activation state controls its light-dependent translocation in rod photoreceptors. *J Biol Chem* 280(49):41069–41076.
22. Majumder A, et al. (2013) Transducin translocation contributes to rod survival and enhances synaptic transmission from rods to rod bipolar cells. *Proc Natl Acad Sci USA* 110(30):12468–12473.
23. Geng Y, et al. (2012) Adaptive optics retinal imaging in the living mouse eye. *Biomed Opt Express* 3(4):715–734.
24. Jian Y, Zawadzki RJ, Sarunic MV (2013) Adaptive optics optical coherence tomography for in vivo mouse retinal imaging. *J Biomed Opt* 18(5):56007.
25. Zawadzki RJ, et al. (2015) Adaptive-optics SLO imaging combined with widefield OCT and SLO enables precise 3D localization of fluorescent cells in the mouse retina. *Biomed Opt Express* 6(6):2191–2210.
26. Zhang P, Goswami M, Zam A, Pugh EN, Zawadzki RJ (2015) Effect of scanning beam size on the lateral resolution of mouse retinal imaging with SLO. *Opt Lett* 40(24):5830–5833.
27. Zhang P, et al. (2015) In vivo wide-field multispectral scanning laser ophthalmoscopy-optical coherence tomography mouse retinal imager: Longitudinal imaging of ganglion cells, microglia, and Müller glia, and mapping of the mouse retinal and choroidal vasculature. *J Biomed Opt* 20(12):126005.
28. Zhang P, Goswami M, Zawadzki RJ, Pugh EN, Jr (2016) The photosensitivity of rhodopsin bleaching and light-induced increases of fundus reflectance in mice measured in vivo with scanning laser ophthalmoscopy. *Invest Ophthalmol Vis Sci* 57(8):3650–3664.
29. Calvert PD, et al. (2000) Phototransduction in transgenic mice after targeted deletion of the rod transducin alpha-subunit. *Proc Natl Acad Sci USA* 97(25):13913–13918.
30. Peinado GA, Fortenbach C, Naarendorp F, Pugh EN, Burns ME (2017) Rapid responses of mammalian rods in vivo are rate-limited by RGS9. *J Gen Physiol*, 10.1085/jgp.201611692.
31. Verkman AS, Ruiz-Ederra J, Levin MH (2008) Functions of aquaporins in the eye. *Prog Retin Eye Res* 27(4):420–433.
32. Li Y, Fariss RN, Qian JW, Cohen ED, Qian H (2016) Light-induced thickening of photoreceptor outer segment layer detected by ultra-high resolution OCT imaging. *Invest Ophthalmol Vis Sci* 57(9):OCT105–OCT111.

33. Sidman RL (1957) The structure and concentration of solids in photoreceptor cells studied by refractometry and interference microscopy. *J Biophys Biochem Cytol* 3(1): 15–30.
34. Heck M, Hofmann KP (2001) Maximal rate and nucleotide dependence of rhodopsin-catalyzed transducin activation: Initial rate analysis based on a double displacement mechanism. *J Biol Chem* 276(13):10000–10009.
35. Kühn H, Bennett N, Michel-Villaz M, Chabre M (1981) Interactions between photoexcited rhodopsin and GTP-binding protein: Kinetic and stoichiometric analyses from light-scattering changes. *Proc Natl Acad Sci USA* 78(11):6873–6877.
36. Lobanova ES, et al. (2008) Transducin gamma-subunit sets expression levels of alpha- and beta-subunits and is crucial for rod viability. *J Neurosci* 28(13):3510–3520.
37. Lobanova ES, et al. (2007) Transducin translocation in rods is triggered by saturation of the GTPase-activating complex. *J Neurosci* 27(5):1151–1160.
38. Kosloff M, Alexov E, Arshavsky VY, Honig B (2008) Electrostatic and lipid anchor contributions to the interaction of transducin with membranes: Mechanistic implications for activation and translocation. *J Biol Chem* 283(45):31197–31207.
39. Sokolov M, et al. (2002) Massive light-driven translocation of transducin between the two major compartments of rod cells: A novel mechanism of light adaptation. *Neuron* 34(1):95–106.
40. Korenbrot JI, Brown DT, Cone RA (1973) Membrane characteristics and osmotic behavior of isolated rod outer segments. *J Cell Biol* 56(2):389–398.
41. Korenbrot JI, Cone RA (1972) Dark ionic flux and the effects of light in isolated rod outer segments. *J Gen Physiol* 60(1):20–45.
42. Russel ES, Bernstein SE (2007) Blood and blood formation. *Biology of the Laboratory Mouse*, eds Green EL, Jackson Lab Staff (Dover, Mineola, NY), 2nd Ed, Chap 17.
43. Renken EM, Curry FE (1978) Transport of water and solutes across capillary endothelium. *Membrane Transport in Biology*, eds Giebisch G, Tosteson DC, Ussing HH (Springer, Berlin), pp 1–45.
44. Kedem O, Katchalsky A (1958) Thermodynamic analysis of the permeability of biological membranes to non-electrolytes. *Biochim Biophys Acta* 27(2):229–246.
45. Kleinhans FW (1998) Membrane permeability modeling: Kedem-Katchalsky vs a two-parameter formalism. *Cryobiology* 37(4):271–289.
46. Preston GM, Carroll TP, Guggino WB, Agre P (1992) Appearance of water channels in Xenopus oocytes expressing red cell CHIP28 protein. *Science* 256(5055):385–387.
47. Prescott DM, Zeuthen E (1953) Comparison of water diffusion and water filtration across cell surfaces. *Acta Physiol Scand* 28(1):77–94.
48. Roof DJ, Heuser JE (1982) Surfaces of rod photoreceptor disk membranes: Integral membrane components. *J Cell Biol* 95(2 Pt 1):487–500.
49. Nickell S, Park PS, Baumeister W, Palczewski K (2007) Three-dimensional architecture of murine rod outer segments determined by cryoelectron tomography. *J Cell Biol* 177(5):917–925.
50. Sułkowska JI, Cieplak M (2008) Stretching to understand proteins - a survey of the protein data bank. *Biophys J* 94(1):6–13.
51. Carvalho FA, Martins IC, Santos NC (2013) Atomic force microscopy and force spectroscopy on the assessment of protein folding and functionality. *Arch Biochem Biophys* 531(1-2):116–127.
52. Zhang X, Wensel TG, Kraft TW (2003) GTPase regulators and photoresponses in cones of the eastern chipmunk. *J Neurosci* 23(4):1287–1297.
53. Kerov V, Artemyev NO (2011) Diffusion and light-dependent compartmentalization of transducin. *Mol Cell Neurosci* 46(1):340–346.
54. Vuong TM, Chabre M, Stryer L (1984) Millisecond activation of transducin in the cyclic nucleotide cascade of vision. *Nature* 311(5987):659–661.
55. Snyder AW, Pask C (1973) Letter: Waveguide modes and light absorption in photoreceptors. *Vision Res* 13(12):2605–2608.
56. Snyder AW, Love JD (1983) *Optical Waveguide Theory* (Chapman & Hall, London).
57. Snyder AW, Menzel R (1975) *Photoreceptor Optics* (Springer, New York).
58. Sihvola A (1999) *Electromagnetic Mixing Formulas and Applications* (Institution of Electrical Engineers, London).
59. Corless JM, Kaplan MW (1979) Structural interpretation of the birefringence gradient in retinal rod outer segments. *Biophys J* 26(3):543–556.
60. Thornburg W (1957) The form birefringence of lamellar systems containing three or more components. *J Biophys Biochem Cytol* 3(3):413–419.
61. Carter-Dawson LD, LaVail MM (1979) Rods and cones in the mouse retina. I. Structural analysis using light and electron microscopy. *J Comp Neurol* 188(2):245–262.
62. Ding JD, Salinas RY, Arshavsky VY (2015) Discs of mammalian rod photoreceptors form through the membrane evagination mechanism. *J Cell Biol* 211(3):495–502.
63. Kalfa TA, Connor JA, Begtrup AH (1993) *EPB42*-related hereditary spherocytosis. *GeneReviews*. Available at https://www.ncbi.nlm.nih.gov/books/NBK190102/. Accessed March 9, 2017.
64. Stewart AK, et al. (2011) Loss-of-function and gain-of-function phenotypes of stomatocytosis mutant RhAG F65S. *Am J Physiol Cell Physiol* 301(6):C1325–C1343.
65. Leskov IB, et al. (2000) The gain of rod phototransduction: Reconciliation of biochemical and electrophysiological measurements. *Neuron* 27(3):525–537.
66. Lamb TD, Pugh EN, Jr (2004) Dark adaptation and the retinoid cycle of vision. *Prog Retin Eye Res* 23(3):307–380.
67. Lyubarsky AL, et al. (2005) Mole quantity of RPE65 and its productivity in the generation of 11-cis-retinal from retinyl esters in the living mouse eye. *Biochemistry* 44(29):9880–9888.
68. Xu J, et al. (1997) Prolonged photoresponses in transgenic mouse rods lacking arrestin. *Nature* 389(6650):505–509.
69. Burns ME, et al. (2006) Deactivation of phosphorylated and nonphosphorylated rhodopsin by arrestin splice variants. *J Neurosci* 26(3):1036–1044.
70. Imai H, et al. (2007) Molecular properties of rhodopsin and rod function. *J Biol Chem* 282(9):6677–6684.
71. Jonnal RS, et al. (2016) A review of adaptive optics optical coherence tomography: Technical advances, scientific applications, and the future. *Invest Ophthalmol Vis Sci* 57(9):OCT51–OCT68.
72. Shevell SK (1977) Saturation in human cones. *Vision Res* 17(3):427–434.
73. Fercher AF, Drexler W, Hitzenberger CK, Lasser T (2003) Optical coherence tomography - principles and applications. *Rep Prog Phys* 66(2):239–303.
74. Wojtkowski M (2010) High-speed optical coherence tomography: Basics and applications. *Appl Opt* 49(16):D30–D61.
75. Jo S, Kim T, Im W (2007) Automated builder and database of protein/membrane complexes for molecular dynamics simulations. *PLoS One* 2(9):e880.
76. Jo S, Lim JB, Klauda JB, Im W (2009) CHARMM-GUI Membrane Builder for mixed bilayers and its application to yeast membranes. *Biophys J* 97(1):50–58.
77. Lomize MA, Lomize AL, Pogozheva ID, Mosberg HI (2006) OPM: Orientations of proteins in membranes database. *Bioinformatics* 22(5):623–625.
78. Miljanich GP, Sklar LA, White DL, Dratz EA (1979) Disaturated and dipolyunsaturated phospholipids in the bovine retinal rod outer segment disk membrane. *Biochim Biophys Acta* 552(2):294–306.
79. Wu G, Hubbell WL (1993) Phospholipid asymmetry and transmembrane diffusion in photoreceptor disc membranes. *Biochemistry* 32(3):879–888.
80. Pettersen EF, et al. (2004) UCSF Chimera–a visualization system for exploratory research and analysis. *J Comput Chem* 25(13):1605–1612.
81. Lyubarsky AL, Daniele LL, Pugh EN, Jr (2004) From candelas to photoisomerizations in the mouse eye by rhodopsin bleaching in situ and the light-rearing dependence of the major components of the mouse ERG. *Vision Res* 44(28):3235–3251.
82. Corless RM, Gonnet GH, Hare DEG, Jeffrey DJ, Knuth DE (1996) On the Lambert W function. *Adv Comput Math* 5(4):329–359.
83. Mahroo OA, Lamb TD (2004) Recovery of the human photopic electroretinogram after bleaching exposures: Estimation of pigment regeneration kinetics. *J Physiol* 554(Pt 2):417–437.
84. Burgoyne T, et al. (2015) Rod disc renewal occurs by evagination of the ciliary plasma membrane that makes cadherin-based contacts with the inner segment. *Proc Natl Acad Sci USA* 112(52):15922–15927.
85. Gross OP, Pugh EN, Jr, Burns ME (2012) Spatiotemporal cGMP dynamics in living mouse rods. *Biophys J* 102(8):1775–1784.
86. Holcman D, Korenbrot JI (2004) Longitudinal diffusion in retinal rod and cone outer segment cytoplasm: The consequence of cell structure. *Biophys J* 86(4):2566–2582.
87. Snyder AW, Pask C (1973) The Stiles-Crawford effect–explanation and consequences. *Vision Res* 13(6):1115–1137.
88. Pask CS, Snyder AW (1975) Angular sensitivity of lens-photoreceptor systems. *Photoreceptor Optics*, eds Snyder AW, Menzel R (Springer, New York), pp 159–174.
89. Okada T, et al. (2000) X-Ray diffraction analysis of three-dimensional crystals of bovine rhodopsin obtained from mixed micelles. *J Struct Biol* 130(1):73–80.
90. Palczewski K, et al. (2000) Crystal structure of rhodopsin: A G protein-coupled receptor. *Science* 289(5480):739–745.
91. Teller DC, Okada T, Behnke CA, Palczewski K, Stenkamp RE (2001) Advances in determination of a high-resolution three-dimensional structure of rhodopsin, a model of G-protein-coupled receptors (GPCRs). *Biochemistry* 40(26):7761–7772.
92. Scheerer P, et al. (2009) Structural and kinetic modeling of an activating helix switch in the rhodopsin-transducin interface. *Proc Natl Acad Sci USA* 106(26):10660–10665.
93. Pascolini D, Blasie JK, Gruner SM (1984) A 12 A resolution X-ray diffraction study of the profile structure of isolated bovine retinal rod outer segment disk membranes. *Biochim Biophys Acta* 777(1):9–20.
94. Schwartz S, Cain JE, Dratz EA, Blasie JK (1975) An analysis of lamellar x-ray diffraction from disordered membrane multilayers with application to data from retinal rod outer segments. *Biophys J* 15(12):1201–1233.
95. Huang W, Levitt DG (1977) Theoretical calculation of the dielectric constant of a bilayer membrane. *Biophys J* 17(2):111–128.
96. Stern HAF, Feller SE (2003) Calculation of the dielectric permittivity profile for a nonuniform system: Application to a lipid bilayer. *J Chem Phys* 118(7):13.
97. Barer R, Joseph S (1954) Refractometry of living cells. 1. Basic principles. *Q J Microsc Sci* 95(4):399–423.
98. Zhao H, Brown PH, Schuck P (2011) On the distribution of protein refractive index increments. *Biophys J* 100(9):2309–2317.
99. Pircher M, Gotzinger E, Leitgeb R, Fercher AF, Hitzenberger CK (2003) Speckle reduction in optical coherence tomography by frequency compounding. *J Biomed Opt* 8(3):565–569.
100. Gao W, Cense B, Zhang Y, Jonnal RS, Miller DT (2008) Measuring retinal contributions to the optical Stiles-Crawford effect with optical coherence tomography. *Opt Express* 16(9):6486–6501.
101. Dithmar S, Curcio CA, Le NA, Brown S, Grossniklaus HE (2000) Ultrastructural changes in Bruch's membrane of apolipoprotein E-deficientmice. *Invest Ophthalmol Vis Sci* 41(8):2035–2042.
102. Hatai S (1918) The refractive index of the blood serum of the albino rat at different ages. *J Biol Chem* 35:527–552.